

Global kinematics study of OH masers in W49N

Mendoza-Torres, J.E.¹, Juárez-Gama M.¹, and Rodríguez-Esnard, I.T.²

¹Instituto Nacional de Astrofísica, Óptica y Electrónica, C. Luis Enrique Erro No. 1, Tonantzintla, Pue. CP 72840, México, e-mail: mend@inaoep.mx

²Instituto de Geofísica y Astronomía, Street 212, No. 2906, between 29 and 31. CP 11600, La Coronela, La Lisa, La Habana, Cuba

Abstract

Star formation is underway in the W49N molecular cloud (MC) at a high level of efficiency, with almost twenty ultra-compact (UC) HII regions observed thus far, indicating a recent formation of massive stars. Previous works have suggested that this cloud is undergoing a global contraction.

We analyse the data on OH masers in the molecular cloud W49N, observed with the VLBA at the 1612, 1665, and 1667 MHz transitions in left circular polarization (LCP) and right circular polarization (RCP) with an aim to study the global kinematics of the masers.

We carried out our study based on the locations and observed velocities of the maser spots, V_{obs} . We found the location $(\alpha, \delta)_m$ of the maximum correlation between $V = V_{obs} - V_{sys}$ (with V_{sys} the systemic velocity) and distance to it. The velocities were fitted to the straight line of $V_{obs} - V_{sys}$ versus $d_{(\alpha, \delta)_m}$, resulting in V_{fid} . The difference between the fitted values and those obtained from observations is $\Delta V = (V_{obs} - V_{sys}) - V_{fid}$. The $V_{obs} - V_{sys}$ velocity shows a gradient as a function of the distance to $(\alpha, \delta)_m$, where the closer spots have the largest velocities. Spots with similar velocities are located in different sectors, with respect to $(\alpha, \delta)_m$. Then, we assumed that the spots are moving towards a contraction centre (CC_{OH}), which is at the apex of a CONUS. We also assumed that the distance of each spot to CC_{OH} is $d_{cc} = \sqrt{2} d_{(\alpha, \delta)_m}$ and that they fall with a velocity $V_{CC} = \sqrt{2} V_{fid}$, with the total velocity being $V_{Tot} = V_{CC} + \sqrt{2} \Delta V$. Using this velocity, we estimated the free-fall velocity.

The coordinates of $(\alpha, \delta)_m$ are effectively $(\alpha_{2000}=19:10:13.1253, \delta_{2000}=9:6:13.570)$. The observed dispersion with respect to the global trend against d_{cc} , shows a maximum at 0.12 pc, with a decay from 0.12 to 0.19 pc, which is faster than that taking place between 0.19 and 0.42 pc. Based on V_{tot} , an inner mass of $M_{inn}=2500 M_{\odot}$ was estimated. In addition, the estimated accretion rate is $\dot{M} = 1.4 \times 10^{-3} M_{\odot} \text{yr}^{-1}$, which requires a time of $t_{inn}=1.8 \times 10^6$ yr to accumulate M_{inn} . The free-fall time, assuming $n=1 \times 10^{-4} \text{cm}^{-3}$, is $t_{ff}=3.4 \times 10^5$ yr. Performing the same procedure with published data that are of lower spatial resolution (than the VLBA data) produces similar results. For example, based on the available data, we find that $(\alpha, \delta)_m = (19:10:13.1392, 9:6:13.4387)$ J2000, which is at $\lesssim 0.3$ asec from what has been calculated with the VLBA data, with an estimated inner mass of $2700 M_{\odot}$. A sub-collapse appears to be taking place in the region traced by the OH maser spots. Based on methanol maser cloudlets data, which lie in a smaller region, another possible centre of contraction is identified, which could be due to a sub-collapse towards a $75 M_{\odot}$ inner mass. The velocities of the OH spots at W49N, along with their positions with respect to $(\alpha, \delta)_m$, make it possible to trace a global kinematics that is apparently due to a sub-collapse in the W49N MC.

1 Introduction

The W49N molecular cloud (MC) is part of the W49A giant molecular cloud, located at a distance of 11.1 kpc (Zhang et al. 2013). The radial velocity of W49N has been estimated to be approximately 8.0 km s^{-1} (Welch et al. 1987). In this region, about 20 HII regions have been observed (Dreher et al. 1984; De Pree et al. 2000, 2004) in different spectral lines (De Pree et al. 1997; Kulczak-Jastrzębska 2017) and in the radio continuum (Wilner et al. 2001; Galván-Madrid et al. 2013). The HII regions, identified by Dreher et al. (1984) as ultra-compact (UC), are thought to be driven by O stars (Wilner et al. 2001), making this region one of the sites at our Galaxy characterised by the active formation of massive stars, with some of them estimated to be $M_* \simeq 25\text{--}35 M_\odot$ and even $M_* \simeq 45 M_\odot$ (Smith et al. 2009).

Masers of OH (Johnston & Hansen 1982; Kent & Mutel 1982; Argon et al. 2000) and of H_2O (Gwinn et al. 1989, 1992; Gwinn 1994; Takefuji et al. 2016) have been observed in W49N. The OH spots detected by Kent & Mutel (1982) with the VLBI have velocities ranging from 4.6 to 21.1 km s^{-1} and Argon et al. (2000) those registered with the VLA, OH spots have velocities between 8 and 22 km s^{-1} . The spots with more red-shifted velocities are mainly located at the west (W), while the less red-shifted appear at the east (E). H_2O maser spots observed by Gwinn et al. (1992) at W49N, have been interpreted as arising at a bipolar outflow of a newly formed star. The spot velocity increases with distance, to a common centre of the flows (denoted by a square in Figure 1), up to velocities greater than 200 km s^{-1} (Gwinn et al. 1992; Gwinn 1994). Each outflow extends about 1 arcsec from their common centre, denoted by a square in Figure 1.

At other sources, the proper motions of OH maser spots have allowed for the local kinematics to be established as likely being due to the expansion of HII regions (Bloemhof et al. 1992; Fish & Reid 2007; Liu et al. 2015), as well as jets (Argon et al. 2003), outflows (Fish et al. 2011), and shells and rings (De Pree et al. 2000).

In W49N, a velocity gradient has been identified, based on a set of HII regions that form a ring (Welch et al. 1987) and it has been suggested that the cloud is in contraction. On the other hand, Serabyn et al. (1993) suggested that the kinematics is due to the collision of two molecular clouds. Rudolph et al. (1990) found inverted P-Cygni profiles in the HCO^+ molecule in W51, which is an association of almost a dozen ultra-compact HII (UC-HII) regions and estimated that it is engaged in a global collapse. They get a mass accretion rate of $\dot{M}=10^{-4} M_\odot \text{ yr}^{-1}$ and an inner mass of $10^5 M_\odot$.

Methanol masers have been seen at W49N (Bartkiewicz et al. 2014; Pandian et al. 2011). They are found to be associated with high-mass star formation (e.g. Sanna et al. 2010a; Moscadelli et al. 2011) and are capable of tracing the kinematics close to the young stellar object (YSO, Moscadelli et al. (2011)). At G16.59–0.05, methanol maser cloudlets trace a rotation around a central mass of about 35 solar mass (Sanna et al. 2010a).

A velocity gradient of each methanol maser cloudlet, V_{grad} , has been seen in a number of sources. Here, the gradient at the cloudlets is compared with the velocity gradient seen at the radial velocity of the cloudlets. From multi-epoch observations, it is found that the velocity gradients and the proper motion vectors point in the same direction in the sky (Moscadelli et al. 2011).

There are still unsolved problems related to the formation of high-mass stars (see Motte et al. 2018; Zinnecker & Yorke 2007). For example, to explain how they can grow to high masses, even under the action of radiation feedback, and how many of them can grow in a given region of a molecular cloud. The latter is known as mass segregation, in hierarchical substructures, the most massive protostellar objects are generally located in the centre of a cluster surrounded by objects of lower mass (Bonnell et al. 2003). One possibility for having many massive stars is that the cores are massive enough when the star formation process begins. The switch-off of the fragmentation process can allow for the conservation of massive cores, which could be due to a slow build-up supported by turbulence or thanks to the stabilisation of massive

clusters for a magnetic field (see McKee & Tan 2002; Commerçon et al. 2011; Myers et al. 2013). Also, as suggested by Welch et al. (1985), the accretion on a global scale, lasting for long timescales, could lead to the accumulation of high masses.

The models applied by Welch et al. (1985) and Rudolph et al. (1990) to interpret the velocity field, as well as the observed masses, agree with the idea that the OB associations are formed by the dynamic collapse of large regions in molecular clouds. A better understanding of the kinematics of the MC W49N will help us to gain a better insight into the processes of star formation and, in particular, the formation of OB associations.

2 Data analysis and results

The data were obtained in the OH lines at the following frequencies: 1667.35903, 1665.4018, and 1612.23101 MHz, hereafter referred to as 1667, 1665, and 1612 MHz, respectively. We are using the same data as Deshpande et al. (2013) with no new calibrations. The observations were made on 6 October 2005, with the Very Long Baseline Array (VLBA) interferometer. Left circular polarization (LCP) and right circular polarization (RCP) are observed simultaneously in about 240 spectral channels with a resolution of 0.1 km s^{-1} in a range of about 22 km s^{-1} . The beam size is about 20 milliarcseconds (mas) by 15 mas at a position angle of 84 degrees. The reference coordinates are $\alpha=19:10:13.2091$ and $\delta = 09:06:12.485$ (J2000).

Table 1: Number of spots recorded at each frequency and polarization.

Freq	LCP	RCP	L+R
1667	73	44	117
1665	42	35	77
1612	6	5	11

To identify maser spots and estimate their flux, central velocity, and coordinates, Astronomical Image Processing System (AIPS) routines were used. In total, 205 spots were identified, in the three observation frequencies at the two polarizations (Table 1 and Figure 1). The size of all the spots is greater than the interferometer beam, indicating that the spots are spatially resolved. The field of the OH spots is at the SW end of the Welch ring of HII regions, in a field made up of about 6 asec sides (Figure 1). The observed velocity of the spots, V_{obs} , is taken respect to the systemic velocity of 8.0 km s^{-1} (Welch et al. 1987) and it spans about 18.6 km s^{-1} . The spots with red-shifted V_{obs} are predominantly located in the W of the map, while the blue-shifted in the E, as reported by Kent & Mutel (1982). This is particularly clear for the frequencies where more spots are seen (1665 and 1667 MHz) at both polarizations (LCP and RCP).

The bipolar outflow lies on the HII region denoted as G1 by De Pree et al. (1997), as also found by Bloemhof (2000). The common centre of the outflows, traced by the H₂O maser spots, becomes – at a location given by an offset in mas of (3110, 380) – relative to the VLBA reference coordinates.

In order to study the global kinematics of the OH spots, we tested the global velocity field to see if it shows a gradient. In spots separated by distances < 1 asec, gradients are observed, however, we did not test single groups of spots, but all the spots across the whole field.

As mentioned above, the OH maser spots that are more red-shifted are in the east, while the less red-shifted ones are in the west. We searched for the possibility that the velocity of the spots versus the distance, with regard to a given location between the groups with different shifts, fits a straight line function. With this purpose, we applied the χ^2 test. The χ^2 error is the sum of squared differences between the values of

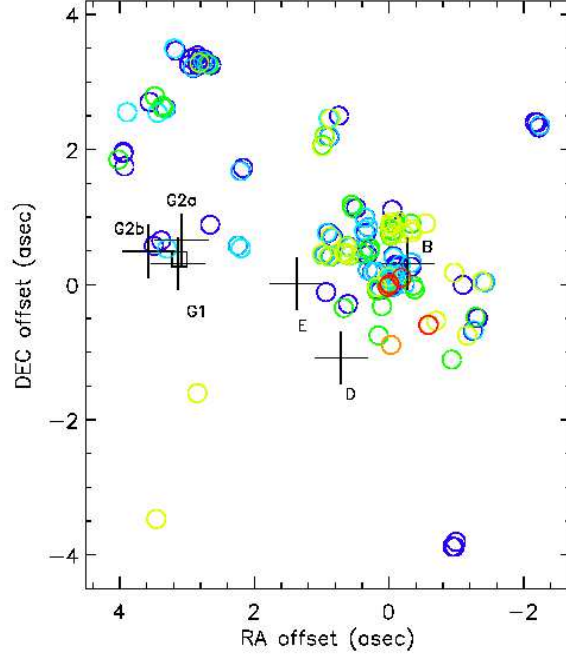


Figure 1: Map of the OH maser spots respect the reference coordinates. The (0,0) location corresponds to $\alpha=19:10:13.2091$, $\delta=09:06:12.485$ (J2000). Respectively, the dark and light blue circles represent the 1667 MHz LCP and RCP maser spots; green and yellow is for 1665 MHz LCP and RCP; and orange and red circles for 1612 MHz LCP and RCP. The crosses indicate the locations of HII regions, reported by [De Pree et al. \(1997\)](#), with the corresponding letters used to refer to each of them. The square that overplots to the cross, which represents G1, corresponds to the location of the centre of the bipolar outflow of [Gwinn et al. \(1992\)](#).

$V_{obs}-V_{sys}$ and those of V_{ftd} , where these last values result from the fit for the distances, d_{ij} , of the spots to the location (α_i, δ_j) , in mas offsets respect the VLBA reference. The smaller the χ^2 value, the better the fit.

We estimated χ^2 for different locations (α_i, δ_j) , regularly separated in both, α and δ , thus forming a mesh. First, we used a mesh that encompasses the whole field of view (FOV) and for each point of the mesh, the test was applied. Based on these results, it is seen that, certainly, in the middle locations of the FOV, χ^2 takes lower values than the rest locations of the FOV. Then, another mesh, with regularly spaced points by $\Delta\alpha = 10$ mas offsets in α and δ (i.e. with respect to the reference coordinates) and in the range, in mas offsets, from 5000 to -4000 in α and from -4500 to 4500 mas in δ is used to identify the minimum value of χ^2 . For each set of d_{ij} distances, the correlation between V_{obs} and d_{ij} was also computed.

We calculated the coefficients of the straight line fitted to $V_{obs}-V_{sys}$ against d_{ij} (we remember that for each point of the mesh, we have a series of distances d_{ij}), obtaining fitted values, V_{ftd} . Since V_{sys} is here considered a constant ($V_{sys}=8.0 \text{ km s}^{-1}$), then the functional relation between $V_{obs}-V_{sys}$ and $d_{(\alpha,\delta)m}$ (seen in Figure 3) is attributed to the value of V_{obs} . Furthermore, we could refer to this functional relation, with the aim to abbreviate the descriptions, by just mentioning V_{obs} and not the whole expression of $V_{obs}-V_{sys}$. The

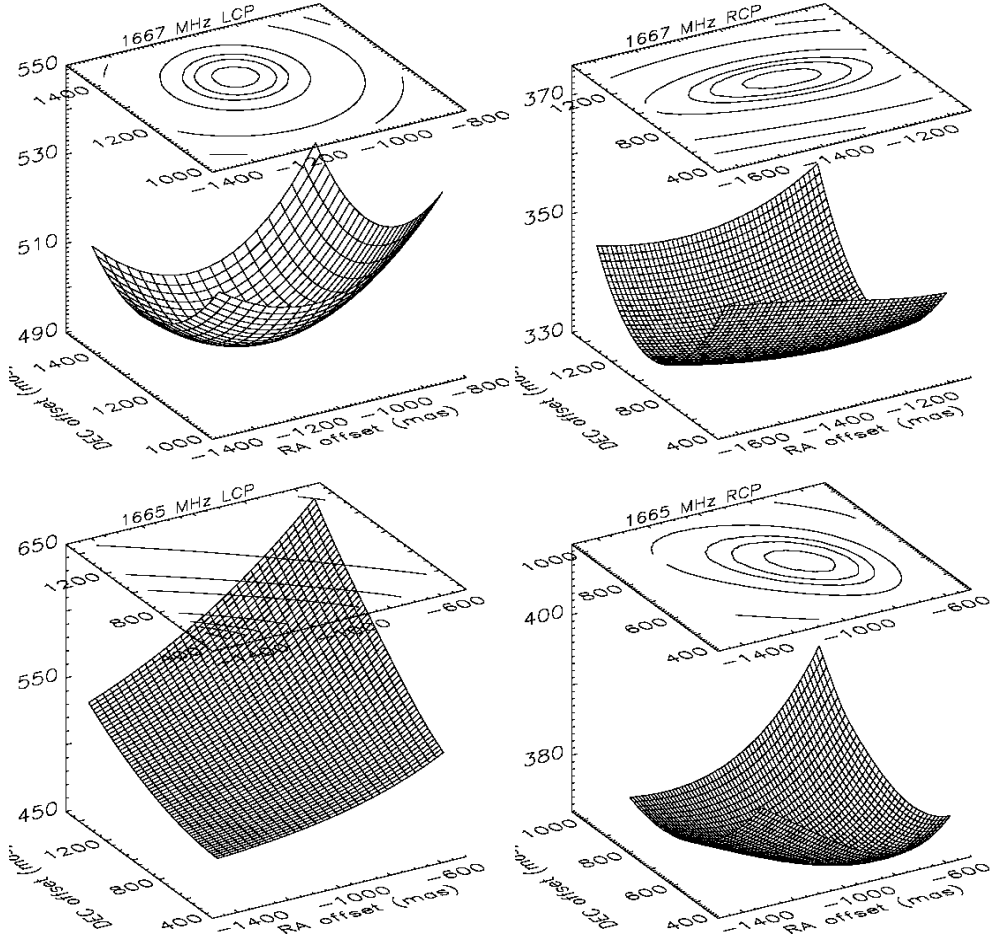


Figure 2: χ^2 values, in contour levels and 3D surfaces around the minimum values for 1667 MHz LCP (top), 1667 MHz RCP (from top to bottom), and 1665 MHz LCP and 1665 MHz RCP (bottom).

difference between the fitted and the observed velocity $\Delta V = (V_{obs} - V_{sys}) - V_{ftd}$ was computed as well as the standard deviation (SD) of ΔV for each testing point.

In Figure 2, the χ^2 values are shown in contour levels and 3D surfaces, around the minimum value. As can be seen from the plots of Figure 2, there is a clear minimum of χ^2 at 1667 LCP and RCP and at 1665 RCP. This means that there is a best fit for a given location for these frequencies and polarizations among all the (α_i, δ_j) values of the mesh. For 1665 LCP, there was not a single minimum of χ^2 . However, as can be seen from Figure 2, the χ^2 values are lower for the zone of the minima at 1667 LCP and RCP, as well as at 1665 RCP. In this zone, the value of correlation (which is the highest at 1665 L) repeats for a number of locations. The same happens for the minimum of χ^2 and the minimum of SD. Then, averaging the coordinates of the highest correlations, we estimated a location that is considered the site of the maximum. For 1612 LCP and 1612 RCP, we did not make the above calculations due to the reduced number of spots (Table 1).

Based on the results of the above analysis, we identified the maximum correlation between V_{obs} and d_{ij} , the minimum of χ^2 and the minimum of the SD. The maximum correlations, for 1667 LCP and RCP and for 1665 LCP and RCP are, respectively, 0.91, 0.87, 0.87, and 0.72. On the other hand, the values of the minimum SD are 2.6, 2.8, 2.8, and 3.6 km s^{-1} (giving them in the same order as the correlations). The maxima of the correlation coincide with the minima of χ^2 and SD. Using the coordinates of the maximum correlation at 1667 LCP and RCP and 1665 LCP and RCP, we calculated the average coordinates, $(\alpha, \delta)_m$, weighted with the number of spots at each frequency and polarization, which turns out to be $(-1236.6, 1085.1)$, relative to the reference coordinates or $\alpha=19:10:13.1253$, $\delta=9:6:13.570$ in J2000.

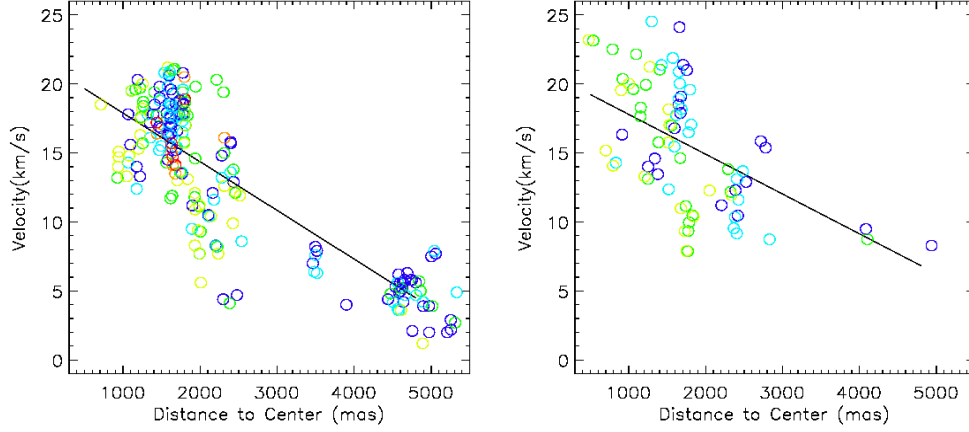


Figure 3: $V_{obs}-V_{sys}$ (with $V_{sys}=8.0 \text{ km s}^{-1}$) versus the distance to the $(\alpha, \delta)_m$ point for the OH VLBA data shown (top). A clear trend is seen, where the velocity grows as the distance $d_{(\alpha, \delta)_m}$ decreases. Same relation but for the VLA data of colour (bottom) taken from Argon et al. (2000). Symbols and colours are the same as in Figure 1.

In the top panel of Figure 3 a plot of $V_{obs}-V_{sys}$ (with $V_{sys}=8.0 \text{ km s}^{-1}$) versus $d_{(\alpha, \delta)_m}$ for the VLBA data is shown. A clear trend is seen, where the velocity grows as the distance $d_{(\alpha, \delta)_m}$ decreases. The velocities of the fitted line will be further referred to as V_{ftd} . For comparison, the Argon et al. (2000) velocity is also plotted with distance (bottom panel of Figure 3), estimated to its reference coordinates (plotted in the same units as for VLBA data). The coordinates $(\alpha, \delta)_m$, relative to the reference, with respect to the OH VLBA observations, are $(-1029.9, 954.1)$, which is at a distance to the point estimated for the VLBA data that is less than 0.3 asec.

The distance histograms have been made by computing the number of spots of LCP and RCP, for a series of distance intervals (or bins, each of 0.2 asec width) to $(\alpha, \delta)_m$, for the data of the three frequencies (top panel of Figure 4). The velocity histogram is shown in the bottom panel of Figure 4. It may be seen that there is no shift, neither in distance nor in velocity, between the LCP and RCP polarizations. In the subsequent steps of the analysis, we included both of them together.

In Figure 5, a map of the spots of all frequencies and polarizations is shown. The asterisk symbol represents the $(\alpha, \delta)_m$ point. The small dashed circle indicates a distance of 1.6 asec to $(\alpha, \delta)_m$, which corresponds to the first maximum of the histogram for distance to $(\alpha, \delta)_m$ for OH masers VLBA data. For the Argon et al. (2000) OH masers VLA data, the first maximum of the histogram also takes place at 1.6

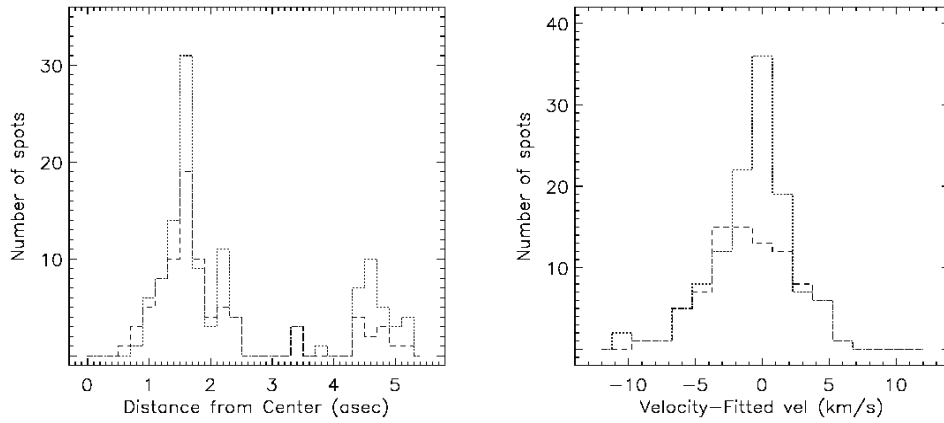


Figure 4: Histogram of the number of spots (including the three frequencies) with the distance to $(\alpha, \delta)_m$, dotted lines are for LCP and dashed for RCP (top). Histogram of the number of spots with velocity (bottom). Lines are as in the top panel.

asec. The subsequent analysis made for VLBA data also leads to similar results with the [Argon et al. \(2000\)](#) VLA data. The large dashed circle corresponds to a distance of 4.6 asec, where the other maximum of the distance histogram (top panel of Figure 4) takes place. The spots in Figure 5, which are around the small circle, appear mostly in the east, but also spots are observed in the north-west (NW) and the south (S), near this circle. The spots around the large circle also appear preferentially in the east and some in the south. Taking the circles in Figure 5 as a reference, it may be seen that the spots are located in various sectors and, without considering the dispersion of shorter spatial scales (< 1 asec), the velocities of spots at equal distances to $(\alpha, \delta)_m$ are similar to each other.

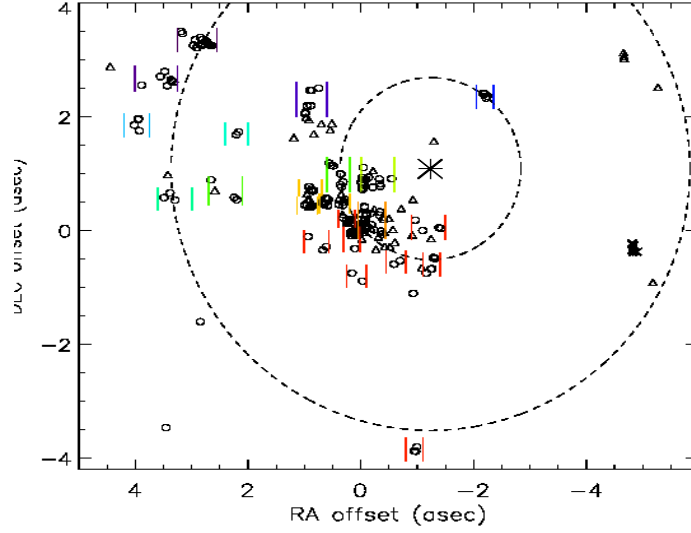


Figure 5: Locations of the OH maser spots, observed with the VLBA, are indicated with small circles. These spots are the same as those plotted in Figure 1 (also with circles). The asterisk represents the $(\alpha, \delta)_m$ point. The groups used to estimate the average velocity (Figure 8) are indicated with vertical bars. The Argon et al. (2000) OH maser spots are indicated with triangles and the methanol maser cloudlets with crosses (\times). All the methanol maser cloudlets that lie in this FOV (Bartkiewicz et al. 2014; Pandian et al. 2011) are on the west side, clumped together near the large dashed circle.

3 Methanol maser cloudlets

We compared the locations of the methanol masers, observed by Bartkiewicz et al. (2014) and by Pandian et al. (2011), in W49N with those of the OH maser spots, and their velocities are analysed to look how they fit in the model proposed for OH spots. The Bartkiewicz et al. (2014) observations were set to four pointing positions. The coordinates (J2000) of the brightest spot at each position are given in their Table 2. The masers detected at W49N are spread over an area of $1.3' \times 0.9'$. In their Table B.1, the locations of the spots are given as angular offsets (in mas) with respect to the location of the brightest spot of each group. The G43.165+00.013 group, which contains 12 spots, is the only one that lies in the FOV of the OH VLBA masers. The coordinates of the brightest spot of this group are $\alpha=19:10:12.882$ and $\delta=09:06:12.2299$. Using the coordinates of this spot and the offsets of the other spots of the group (with respect to the former), we obtained their corresponding α and δ (J2000). Then, with these coordinates and the coordinates of the OH reference point ($\alpha=19:10:13.2091$, $\delta=09:06:12.485$), the spot coordinates were transformed to offsets, but now with respect to the OH VLBA reference.

The Pandian et al. (2011) methanol maser observations also were made to different pointing positions, whose locations span to more than $1'$ in both, α and δ . The locations of the spots are given in absolute coordinates in their Table 3. Only the G43.16+0.02 maser spot, lies in the FOV of the OH masers. Its location coincides with the above-mentioned Bartkiewicz et al. (2014) group (bottom panel of Figure 6).

To transform these coordinates into offsets, with respect to the OH reference point, we subtracted the

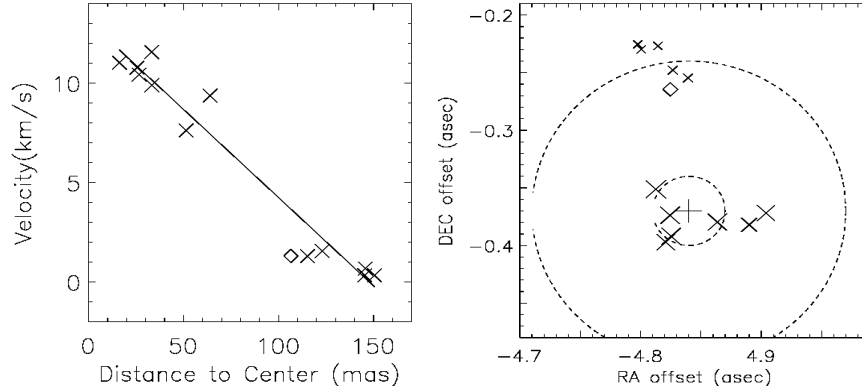


Figure 6: Crosses indicate the $V_{pk}-V_{sys}$ velocities against the $d_{(\alpha,\delta)mMeth}$ distances (to the point $C_{(\alpha,\delta)mMeth}$) of the methanol cloudlets observed by Bartkiewicz et al. (2014), shown at the top. The rhombus indicates the $V_{pk}-V_{sys}$ velocity against $d_{(\alpha,\delta)mMeth}$ of the Pandian et al. (2011) spot that lies in this FOV. Crosses (x) indicate the locations of the Bartkiewicz et al. (2014) methanol cloudlets and the rhombus, as well as the Pandian et al. (2011) methanol cloudlet, all of them given as offsets in asec, with respect the OH VLBA reference coordinates, shown at the bottom. The size of the symbols is proportional to the velocity. The cross (+) indicates the location where the maximum correlation between $V_{pk}-V_{sys}$ and the distance $d_{(\alpha,\delta)mMeth}$ is attained. The distance, $d_{(\alpha,\delta)mMeth}$, used in the top-panel plot is computed from this point. Dashed circles are plotted for reference at 30 and 130 mas from $C_{(\alpha,\delta)mMeth}$.

OH reference coordinates from the Pandian et al. (2011) coordinates of the spot.

The observations of Bartkiewicz et al. (2014) were made with a very high angular resolution (of ~ 5 mas). Among the parameters that they report, here we use the above-mentioned offsets (RAoffset, Decoffset), the velocity of the peak flux (V_{pk}) and the velocity gradient (V_{grad}), all of them for each spot. The last parameter is the velocity variation at the different velocity channels, where the spot is detected, with respect to the coordinates at these velocities.

In Figure 5, the locations of the methanol maser cloudlets are represented with crosses. The spots of both, Bartkiewicz et al. (2014) and Pandian et al. (2011) data are clumped together in the west, near the large dashed circle.

The OH VLBA field is $6'' \times 6''$, which is small compared to the whole area of the Bartkiewicz et al. (2014) spots at W49N and of the field of the Pandian et al. (2011) one. This is to say that even if the distance between the centres of the fields is approx $5''$, the methanol fields are much larger than the OH one and many of the methanol cloudlets, as reported by Bartkiewicz et al. (2014) and by Pandian et al. (2011) lie outside the field of the OH spots.

The peak velocities, V_{pk} , of the Bartkiewicz et al. (2014) maser spots spread from about 8 to 20 km s^{-1} . The range of velocities and the high spatial resolution allows us to do the same process as that for OH spots. A mesh of points, separated $\Delta\alpha=10$ mas, from -4500 to -5100 mas in right ascension (RA) and separated $\Delta\delta=10$ mas from -600 to 0 mas in Declination (Dec) was used. The correlation and the χ^2 between V_{pk} and distance are estimated to each point of the mesh for the 12 spots mentioned by Bartkiewicz et al. (2014). We further refer to $C_{(\alpha,\delta)mMeth}$ as the point for which the highest correlation is attained. In the top panel of Figure 6, we show a plot of $V_{pk}-V_{sys}$, with $V_{sys}=8 \text{ km s}^{-1}$, where the systemic velocity estimated by Welch et al. (1987) against the distance (d_{ccMeth}) to $C_{(\alpha,\delta)mMeth}$ is shown. It may be seen that the velocity

undergoes a gradient with a negative slope (as in the case of OH masers). Similarly to the procedure with OH data, a straight line with velocity V_{ftd} is fitted to these data. The $V_{pk}-V_{sys}$ against distance to $C_{(\alpha,\delta)mMeth}$ values for the Pandian spot are also plotted with a rhombus.

In the bottom panel of Figure 6, the locations of the methanol maser cloudlets of the G43.165+00.013 group from Bartkiewicz et al. (2014) are indicated by crosses (\times). The sizes of the symbols are proportional to the $V_{pk}-V_{sys}$ velocities. The rhombus in the N corresponds to the Pandian et al. (2011) spot. The point $C_{(\alpha,\delta)mMeth}$ is indicated with the plus symbol (+). The dashed circles are plotted for reference at distances from $C_{(\alpha,\delta)mMeth}$ (30 and 130 mas), where more spots are seen. It may be seen from the bottom panel of Figure 6 that the spots closer to $C_{(\alpha,\delta)mMeth}$ have higher velocities than the spots farther from it. Additionally, it is seen that spots located at different sectors of the small dashed circle have similar $V_{pk}-V_{sys}$ velocities. The velocity field indicates acceleration towards $C_{(\alpha,\delta)mMeth}$.

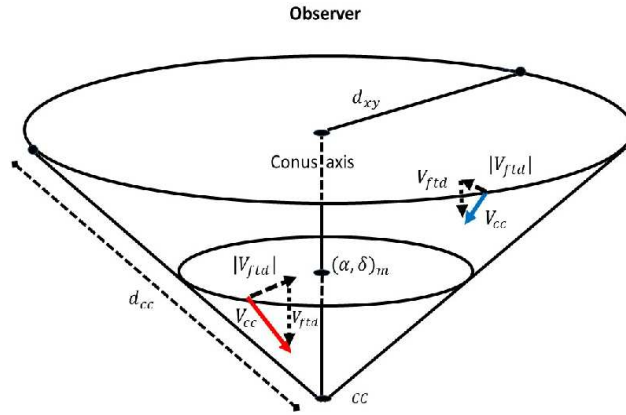


Figure 7: Model of the contraction velocities, V_{cc} , of the OH spots, i.e. of their velocities towards a common centre of contraction (CC). V_{ftd} (represented with dotted lines) corresponds to the velocity from the straight line fitted to the observed data for the given distance to $(\alpha, \delta)_m$, as may be seen in Figure 3. This velocity is assumed to be the radial component of the contraction velocity. Each spot has its own velocity (the two V_{ftd} , represented here, are different to each other in magnitude). The small ellipse corresponds to the small circle plotted in Figure 5. For an assumed spot at a point in this circle, $|V_{ftd}|$ is the magnitude of the transversal velocity, which is directed to the CONUS axis (and orientated perpendicular to it). The $|V_{ftd}|$ of the spot at the large ellipse is smaller than that at the small one. The resulting contraction velocity, of a magnitude, V_{cc} , lies on the surface of the CONUS and it is directed to the CC point (the apex of the CONUS).

4 Discussion

The velocity field in 3D could be reconstructed by using both the radial velocity, V_{obs} , and the proper motions of the spots. However, in this case, we did not have access to this last information. Nevertheless, the fact that there is a region, in the field, for which the correlation between V_{obs} and the distance to that region, $d_{(\alpha,\delta)_m}$, takes the largest values, among all the points of the field; this indicates that the behaviour of the velocity field is more clearly revealed because it is probably a location the behaviour of this velocity field is dependent on. In other words, it is a parameter involved in a functional relationship between V_{obs} and $d_{(\alpha,\delta)_m}$.

For Keplerian rotation, the velocities in the E and W sectors, with respect to the systemic velocity, are opposite to each other and the velocities in the N and S are near to the value of the systemic velocity, as can be seen at single sources. From Figures 3 and 5, it may be seen that none of these characteristics is present in the OH spots in W49N. Nevertheless, a series of tests of the locations and velocities of the sources was made with a geometric method, which allows us to compare them with ellipses, which are due to inclined Keplerian rotation orbits (Rodríguez-Esnard 2011). In Appendix A, the bases of the method to test the fit of the spots to an ellipse are given. Applying it to OH maser data, it is found that only nine spots of the 1665 LCP and ten spots of the 1665 RCP provide a good fit to ellipses for Keplerian-rotation. However, the geometric elements of the ellipses (centre, major axis and eccentricity) differ considerably from each other. Finally, we conclude that the spots are not in a rotating disk.

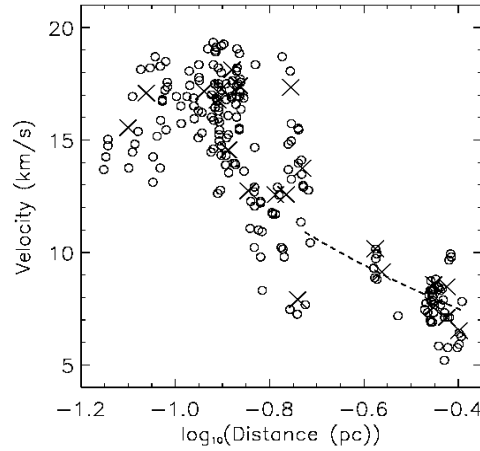


Figure 8: Estimated total velocity, V_{Tot} , of the OH spots to the centre of contraction, as a function of the distance to CC, d_{cc} . The crosses (x) denote the average velocities for the groups indicated with bars in Figure 5. The dashed line denotes the free fall velocity for $M_{inn}=2500 M_{\odot}$.

It has been seen that V_{obs} shows a general trend along the whole field, indicating that the velocity of the masers, in this field, has a global component. With respect the $(\alpha, \delta)_m$ point, the spots are predominantly in the E sector, distributed in an elongated shape, NE–WS orientated. In other sources, accretion has been seen to take place through filaments (Peretto et al. 2013). However, the amount of material accreted through them is not as large as the amount accreted radially. In the case of the W49N, the highest correlation is observed between V_{obs} and d_{ij} (the distance to the point $(\alpha, \delta)_m$) and not along the direction of the elongation. The OH spots with similar velocities are approximately at the same distance to $(\alpha, \delta)_m$. For example, as above mentioned, the spots that are close to the reference circle plotted at 1.6 asec radius have similar velocities,

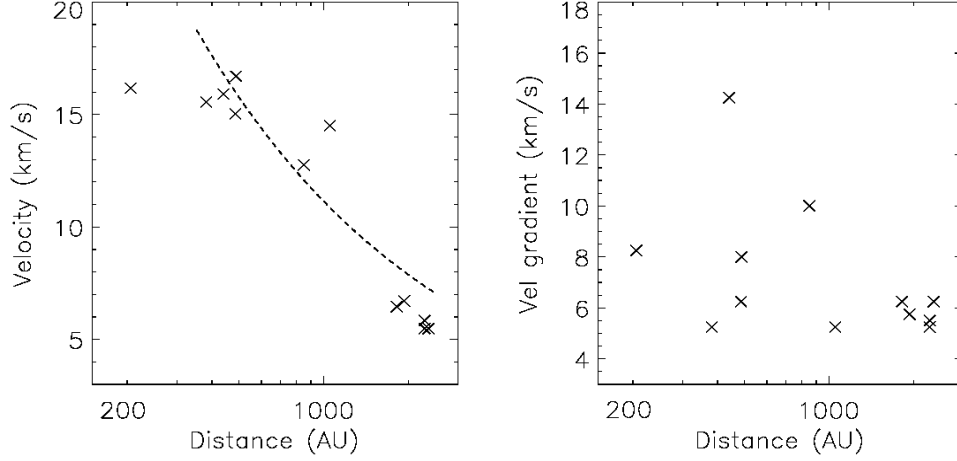


Figure 9: Velocity V_{TMeth} versus the distance, of each methanol cloudlet seen at the W in Figure 5, to d_{ccMeth} shown on top. The dashed line corresponds to the free-fall velocity for a $75 M_{\odot}$ inner mass. The V_{grad} velocity of each methanol cloudlet versus the d_{CCMeth} distance (bottom).

although they are in different sectors. For the spots around the circle at 4.6 asec, the same situation is seen but these spots have lower velocities. The spots are likely in a global velocity field, which is consistent with an accelerating contraction towards the $(\alpha, \delta)_m$ point; this can be interpreted as global contraction towards a common centre (CC). The results obtained with VLBA observations are supported by the [Argon et al. \(2003\)](#) data, obtained with the VLA, the $(\alpha, \delta)_m$, as these data only differ by 0.3 asec with respect to the point estimated with the VLBA data.

4.1 3D model of the contraction velocities

We recall that V_{ftd} has a functional relation (fitted line in Figure 3) to the distance to $(\alpha, \delta)_m$. The shorter the distance to $(\alpha, \delta)_m$ the greater the V_{ftd} . Then, given the distance to $(\alpha, \delta)_m$, the corresponding V_{ftd} velocity can be known. It is the same for all the points on a circle centred at $(\alpha, \delta)_m$. These velocities can then be further used for the purposes of building a model. In Figure 7, the V_{ftd} velocity for two spots, one assumed to be at the distance of the small and the other of the large circles of Figure 5 are shown. Each V_{ftd} is considered to be the radial component of the contraction velocity to a common centre (V_{cc}). They differ from one another in magnitude and, ultimately, that the spot that is closer to CC has higher V_{ftd} velocity than the spot that is farther from it. We consider the possibility that the CC is not on the same plane of the small circle (at Figure 5). We assume that the V_{cc} of the two plotted spots and of all the spots are directed towards CC, which is at the apex of a CONUS, and all the V_{cc} vectors are located on the surface of the CONUS.

In the model, d_{xy} is the distance from a spot to the CONUS axis (Figure 7). In particular, for the plane of the small circle, this distance is equal to $d_{(\alpha, \delta)_m}$. Furthermore, the XY-plane of the small circle will be considered as a reference. It is represented with the small ellipse in Figure 7. The distance to this plane is d_z , it is positive as going farther from the observer and negative as it gets closer to the observer. In terms of the observed values, it may be seen that the spots that are at distances < 1.6 asec, that is, closer to CC with respect to the small circle and farther from the observer would be at $d_z > 0$; the spots that are at distances > 1.6

asec, namely, farther from CC and closer to the observer would be at $d_z < 0$ (Figure 7). The CC is in the line of sight of the point $(\alpha, \delta)_m$ at a distance, d_{z0} . The angle between the CONUS axis and the line from a spot to the CC is indicated with θ .

The tangential component of V_{cc} is unknown. Then, for the model, the following assumptions are as follows: 1) the tangential component of V_{cc} follows the same functional relation with the distance as the radial component with the distance to $(\alpha, \delta)_m$. We remember that in the z -direction, the distance to CC is d_z (Figure 7); 2) it is orientated perpendicular to the CONUS axis and it directed to it. In the case of spots on the small circle of Figure 7, this velocity is pointing to $(\alpha, \delta)_m$. 3. It can be considered, for simplicity, that the tangential component of V_{cc} has a magnitude equal to $|V_{fid}|$. In the representation of Figure 7, each point on the CONUS has its own velocity $V_{fid}(\hat{z})$, pointing in a radial direction (respect the observer) and their own tangential velocity, $|V_{fid}|(\hat{r})$ (pointing to the CONUS axis), and the vector \vec{V}_{cc} would be the sum of them. Furthermore, these velocities are not written in vectorial notation, since in the model, each of them displays a clear orientation and sense, as may be seen from Figure 7.

With the above-listed conditions on the contraction velocities, we can assume that the distance of a spot to the CONUS axis (d_{xy}), which is measured perpendicular to the axis, would be the same as the distance in the radial direction (d_z) and thus $\theta=45^\circ$. This means that for the plotted spots (and any spot overall even if it does not lie at any of the two circles), the result will be $d_z=d_{xy}$. The distance of each spot to CC is thus $d_{cc} = \sqrt{2} d_{xy}$. The distance, d_{cc} , is measured from CC to the spot. In the model (Figure 7), the distance, d_{cc} , to a spot that lies within the dashed circle, namely, at a distance of 1.6 asec, is indicated. If another spot does not lie at this distance, then it will not be at the dashed circle; however, it will be over the CONUS and its infalling velocity (due to global contraction) that is given for the linear fit of Figure 3. The tangential velocity also depends on θ , which is the aperture of the CONUS. For $\theta=45^\circ$, its magnitude is $|V_{fid}|$ and then $V_{cc} = \sqrt{2} V_{fid}$.

Besides the V_{cc} values, the velocity of each spot also could have random or local kinematics components. However, the difference $\Delta V = (V_{obs} - V_{sys}) - V_{fid}$ (Figure 3) represents only the radial component of this velocity. To include a reasonable input to the random or local kinematics velocity in a tangential direction, we compute it in the same way as for V_{fid} . Then, taking into account that $\theta = 45^\circ$, the estimation of a total velocity for each spot leads to $V_{tot} = V_{cc} + \sqrt{2} \Delta V$. The total velocity is plotted in Figure 8.

The average velocity of groups of spots located near each other is an estimate of the group velocity and this would reduce the impact of local kinematics or random velocities in the data dispersion. This could allow us to see how the group velocity versus d_{cc} would behave, with regard to the case of separated spots. The groups of spots that we used are indicated with the vertical lines in Figure 5. The average of the velocity of each group is shown with diamonds in Figure 8, together with the velocity of separated spots (crosses). It may be seen that they behave similarly to each other, showing a maximum at about $\log(d_{cc}) = -0.9$ (~ 0.12 pc). A general velocity increase is seen, which is rather noisy nonetheless, as a trend from 0.19 to 0.12 pc. On the other hand, a general decrease from 0.12 pc to shorter distances is also seen. For the computation of the infall velocity field, we considered the 0.42-0.19 pc interval. For the infall velocity, we use the value fitted to $V \sim d_{cc}^{-0.5}$ at 0.19 pc, which is 10.7 km s^{-1} .

We recall that the velocity difference (ΔV) is the result of subtracting the fitted velocity, given by the straight line of Figure 3 from the observed velocity. Therefore, ΔV is related to components, of the spot velocity, which is different to the infalling velocity. In Figure 10, the velocity difference, ΔV versus V_{obs} is plotted. The closer a spot is to CC , the smaller the symbol that represents its velocity. Different symbols correspond to spots at different distance intervals. The spots grouped in a given distance interval are fitted by the same straight line. This occurs even though the spots are located at different sectors with respect to a centre point, which in this case, is CC . The small crosses represent the closest spots to $(\alpha, \delta)_m$, while

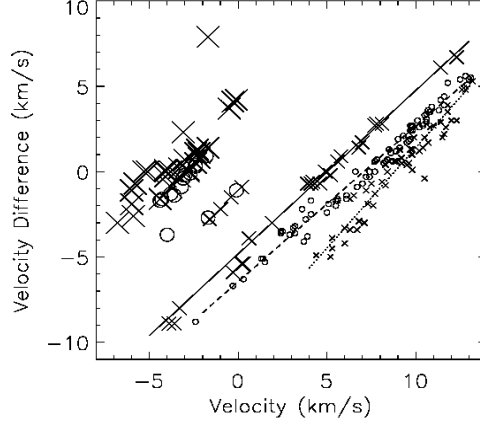


Figure 10: Velocity difference (ΔV) versus V_{obs} . Different symbols correspond to spots at different distance intervals. The small crosses are for $d_{cc} < 0.09$ pc, the dashed line is fitted to these spots. The small circles are for spots at $0.09 \text{ pc} < d_{cc} < 0.12$ pc, and the dotted line is fitted to them. The continuous line is fitted to spots at $0.12 \text{ pc} < d_{cc} < 0.19$ pc, which is shown with mid-size crosses. The large circles are for $0.19 \text{ pc} < d_{cc} < 0.25$ pc and large crosses for $0.25 \text{ pc} < d_{cc} < 0.42$ pc.

small circles represent the spots that are next in terms of the distance and so on. The spots around the continuous line correspond to the velocity increase seen from 0.19 to 0.12 pc. As may be seen from this figure, these lines show the largest velocity dispersion. They belong to different groups of Figure 5, some of them located in the east, others in the south, and some in the north-west. The spots at $d < 0.12$ pc also belong to various groups of Figure 5 in different sectors. They seem to be experiencing a deceleration as approach CC (Figure 8). This could be similar to the case of a single protostar model (Stahler et al. 1980) in the sense that it could be accretion in a structured shape, including different layers. In the case of global collapse, there is no such detailed scheme. However, here we do not attempt to study these details in this work.

To estimate the free fall time, we assumed $n = 1 \times 10^{-4} \text{ cm}^{-3}$ and an average mass particle $\langle m \rangle = 2.33 m_H$ (Kauffmann et al. 2008, 2013), obtaining a result of $t_{ff} = 3.4 \times 10^5 \text{ yr}$. The accretion rate, assuming a spherical geometry, can be calculated from $2\pi r \rho V_{infall}$, for a distance of 0.19 pc and ρ from the above estimation, we have an accretion rate of $1.4 \times 10^{-3} M_{\odot} \text{ yr}^{-1}$. Considering this accretion rate, the time required to accumulate a mass of $2500 M_{\odot}$ is 1.8×10^6 years, which is 5.2 times t_{ff} .

Part of the inner mass is in the cores and stars embedded in HII regions. Smith et al. (2009) found that several radio sources are deeply embedded inside the cloud core. Also, part of the mass could take the form of stars that already have swept out their HII regions and could be not detectable in the radio continuum and other wavelengths.

To estimate the virial coefficient, it must be taken into account that the velocity dispersion is due to global and to local kinematics. We calculated the virial mass, M_{vir} , using the standard deviation of ΔV , which turns out to be 2.9 km s^{-1} and leads to $M_{vir} = 380 M_{\odot}$. It is smaller in more than six times M_{inn} , which is the mass obtained by fitting the free-fall function to the V_{cc} values.

Rudolph et al. (1990) estimated a global collapse in W51 with a mass of $4 \times 10^4 M_{\odot}$ and a $1200 M_{\odot}$ subcollapse. The field of the OH spots in W49N has a size of approximately $\sim 7 \text{ asec}$, while the ring of

Welch et al. (1985) for W49N is ~ 20 asec. This means that the smaller region is virialized by itself, even though it is a fraction $\sim (7/20)^3$ of the Welch ring of HII regions. However, the kinematics of the smaller region spans a velocity range similar to the velocity range of the ring. The global velocity field of OH masers could be due to a sub-collapse similar to that observed in W51.

The analysed group of methanol cloudlets show similar conditions, in velocity and location, to those seen in the OH masers, allowing us to apply them to the same model (with another centre of contraction). It should be noted, however, that only one OH maser spot (indicated with a circle in the right panel of Figure 6) is co-spatial to the methanol cloudlets. This means that the OH spots do not trace this region. Sanna et al. (2010b) studied the high-mass star-forming region G23.01-0.41 and found that the OH spots are more distant from the YSO than the methanol ones. Here, the only OH spot, which is co-spatial to this group, is certainly in the external region with respect to CC_{Meth} .

The velocity gradient, seen at a group of methanol cloudlets, could be related to the kinematics of the source. In the top panel of Figure 9, the velocity gradient, V_{grad} , of each spot is plotted against its distance to CC_{Meth} . It may be seen that the values of V_{grad} at ~ 500 AU (near to the small dashed circle) have a larger dispersion than the spots at ~ 2000 AU (near to the large dashed circle). We should not exclude the possibility that near to CC_{Meth} , another kinematical component, such as a disk, jet, or outflow that has been traced in other sources with methanol masers (Pandian et al. 2011; Moscadelli et al. 2011), could be present. That scenario would lead to larger dispersion in the velocity field in this region and a larger difference in the velocity from one spot to another than in regions that undergo a single type of kinematics.

Only one Pandian et al. (2011) methanol maser cloudlet lies in the field of OH spots, which is coincident with the Bartkiewicz et al. (2014) methanol cloudlets. They are located in the west of the VLBA field (crosses (x)). The velocity of the Pandian et al. (2011) spot is $V_{pk}=9.3 \text{ km s}^{-1}$ which, taking into account $V_{sys}=8 \text{ km s}^{-1}$, gives us $V_{pk}-V_{sys}=1.3 \text{ km s}^{-1}$. This velocity is similar to those of the OH spots located at similar distances from CC_{OH} . The values (velocity and distance) for this spot are also plotted in Figure 6. The rhombus that represents it (in the top panel) lies near the straight line fitted to the velocity versus distance plot, for the Bartkiewicz et al. (2014) spots.

4.2 Contraction of the group of methanol maser cloudlets

Velocity gradients are expected to be observed in different kinematical models. In the case of maser spots in a rotating disk, the spots with more red- and more blue-shifted velocities would be observed, from the Earth, at both sides of the central region. The locations at W49N of methanol cloudlets with similar velocities, in different sectors (small dashed-circle of the right panel of Figure 6), differ from what is expected in a rotating disk. Instead, this indicates that another type of kinematics is responsible for spots with such velocities and locations. The expansion or contraction is suitable to explain both conditions, with respect to a given centre. A third condition, namely, the larger velocities seen closer to the $C_{(\alpha,\delta)mMeth}$ point, agree with accretion in an accelerated velocity field.

The velocity versus distance relation of the methanol maser cloudlets seen at the FOV of the OH VLBA maser spots (Figure 6) also suggests a centre of contraction for this particular group. A model of contraction is applied in a similar way as in the case of OH spots (Section 4.1 and Figure 7). We assume that the distance in the direction perpendicular to the XY-plane, from each spot to CC_{Meth} , is the same as the distance, $d_{(\alpha,\delta)Meth}$, from the spot to $C_{(\alpha,\delta)mMeth}$. Then, the distance of each spot to this point is $d_{ccMeth} = \sqrt{2} d_{(\alpha,\delta)Meth}$ and we consider that the total velocity is $V_{TMeth} = \sqrt{2}V_{fth} + \sqrt{2}\Delta V_{Meth}$. The first term corresponds to the falling velocity (towards CC_{Meth}) and the second to the dispersion velocity, with respect to the falling one.

In the top panel of Figure 6, the velocity, V_{TMeth} , is plotted against d_{ccMeth} . Taking the interval of distances from 300 to 2500 AU, a free-fall function is fitted to $V_{pk}-V_{sys}$ versus d_{ccMeth} (dashed line in the

top panel of Figure 9), obtaining an inner mass of $75 M_{\odot}$. This approximation helps us to estimate the inner mass, under the assumption of accretion. In this case, it is a region on a smaller spatial scale than that of the OH maser spots, indicating the possibility of another sub-collapse (that could contain various forming stars or one massive forming star).

The amount of methanol cloudlets in the W49N field, where the OH masers are seen, is smaller than the OH spots number. The methanol cloudlets are at given locations of the whole region, while the OH ones are more spread, namely, they appear in more locations across the region. This result agrees with the previous finding that 6.7 GHz methanol masers trace early phases of the high-mass star formation process (Minier et al. 2005; Pandian et al. 2011). The methanol masers could be more suitable to trace the velocity of the environment of such objects, providing the opportunity to study their kinematics. This also indicates that the OH and methanol masers seem to be complementary to each other in the study of star formation rates (SFR, (Sanna et al. 2010b)).

The locations and velocities of methanol masers do not disagree with a scenario of a subcollapse in W49N, as deduced from OH masers. Moreover, their velocities and locations agree with accretion scenarios at shorter spatial scales, which could indicate the possibility of sub-collapses on these scales. The combination of both maser species, therefore, seems to be a tool that is useful in building a more complete picture of the kinematics of SFR on different spatial scales, particularly in large complexes such as W49N.

As opposed to the case of the OH and the methanol maser spots analysed here, which trace contractions, the H_2O maser spots at W49N, trace outflows. The bipolar outflow is related to the local kinematics at the G1 HII region and the velocity range of the H_2O maser spots is considerably larger than the global field velocity range estimated by Welch et al. (1985) and also for the one analysed here. This means the H_2O spots are related to local conditions at a given HII region, while the OH maser spots are related to the global kinematics.

5 Conclusions

The maximum correlation between the observed velocity, V_{obs} , and the distances to test points, d_{ij} , takes values larger than 0.7 for 1665 (RCP and LCP) and 1667 (RCP and LCP). Using the distance of the spots to the weighted average coordinates $(\alpha, \delta)_m$, of the maxima of the correlation, the location of the projection of the centre of contraction to the XY-plane is estimated as $(\alpha_{2000}=19:10:13.1253, \delta_{2000}=9:6:13.570)$. It is found that the behaviour of $V_{Tot}=V_{cc} + \sqrt{2} \Delta V$ against d_{cc} shows a maximum at 0.12 pc, with a decrease from 0.12 to 0.19 pc that takes place faster than the decrease between 0.19 and 0.42 pc. Assuming that the behaviour of the velocity at the 0.19 and 0.42 pc interval is due to free fall accretion, an inner mass of $M_{inn}=2500 M_{\odot}$ is obtained. We estimate the accretion rate to be $\dot{M}=1.4 \times 10^{-3} M_{\odot} \text{yr}^{-1}$ which requires a time $t_{inn}=1.8 \times 10^6$ yr to accumulate M_{inn} . The velocities of the OH spots at W49N, together with their positions with respect to the $(\alpha, \delta)_m$ point, makes it possible to estimate the spot kinematics. Finally, this can be interpreted as a contraction of the cloud that appears to be a sub-collapse in the W49N MC.

6 Acknowledgements

We would like to thank the Astrophysics Department of INAOE for its financial support. M-T J.E. would like to acknowledge M. Goss for providing the VLBA data of 2005. We also thank the anonymous referee for her/his careful review of the present article and helpful suggestions, which have been very useful to us for improving this work.

Bibliography

- Argon, A. L., Reid, M. J., & Menten, K. M. 2000, *ApJS*, 129, 159. doi:10.1086/313406
- Argon, A. L., Reid, M. J., & Menten, K. M. 2003, *ApJ*, 593, 925. doi:10.1086/376592
- Bartkiewicz, A., Szymczak, M., & van Langevelde, H. J. 2014, *A&A*, 564, A110. doi:10.1051/0004-6361/201322629
- Bloemhof, E. E., Reid, M. J., & Moran, J. M. 1992, *ApJ*, 397, 500. doi:10.1086/171807
- Bloemhof, E. E. 2000, *ApJ*, 533, 893. doi:10.1086/308714
- Bonnell, I. A., Bate, M. R., & Vine, S. G. 2003, *MNRAS*, 343, 413. doi:10.1046/j.1365-8711.2003.06687.x
- Commerçon, B., Hennebelle, P., & Henning, T. 2011, *ApJ*, 742, L9. doi:10.1088/2041-8205/742/1/L9
- De Pree, C. G., Mehringer, D. M., & Goss, W. M. 1997, *ApJ*, 482, 307. doi:10.1086/304119
- De Pree, C. G., Wilner, D. J., Goss, W. M., et al. 2000, *ApJ*, 540, 308. doi:10.1086/309315
- De Pree, C. G., Wilner, D. J., Mercer, A. J., et al. 2004, *ApJ*, 600, 286. doi:10.1086/379755
- Deshpande, A. A., Goss, W. M., & Mendoza-Torres, J. E. 2013, *ApJ*, 775, 36. doi:10.1088/0004-637X/775/1/36
- Dreher, J. W., Johnston, K. J., Welch, W. J., et al. 1984, *ApJ*, 283, 632. doi:10.1086/162348
- Fish, V. L. & Reid, M. J. 2007, *ApJ*, 670, 1159. doi:10.1086/522329
- Fish, V. L., Gray, M., Goss, W. M., et al. 2011, *MNRAS*, 417, 555. doi:10.1111/j.1365-2966.2011.19297.x
- Galván-Madrid, R., Liu, H. B., Zhang, Z.-Y., et al. 2013, *ApJ*, 779, 121. doi:10.1088/0004-637X/779/2/121
- Gwinn, C. R., Moran, J. M., Reid, M. J., et al. 1989, *The Center of the Galaxy*, 136, 47
- Gwinn, C. R., Moran, J. M., & Reid, M. J. 1992, *ApJ*, 393, 149. doi:10.1086/171493
- Gwinn, C. R., Bartel, N., & Cordes, J. M. 1993, *ApJ*, 410, 673. doi:10.1086/172784
- Gwinn, C. R. 1994, *ApJ*, 429, 253. doi:10.1086/174316
- Johnston, K. J. & Hansen, S. S. 1982, *AJ*, 87, 803. doi:10.1086/113159
- Johnston, K. J. & Hansen, S. S. 1982, *AJ*, 87, 803. doi:10.1086/113159
- Kauffmann, J., Bertoldi, F., Bourke, T. L., et al. 2008, *A&A*, 487, 993. doi:10.1051/0004-6361:200809481
- Kauffmann, J., Pillai, T., & Goldsmith, P. F. 2013, *ApJ*, 779, 185. doi:10.1088/0004-637X/779/2/185
- Kent, S. R. & Mutel, R. L. 1982, *ApJ*, 263, 145. doi:10.1086/160489
- Kulczak-Jastrzębska, M. 2017, *ApJ*, 835, 121. doi:10.3847/1538-4357/835/2/121
- Liu, T., Kim, K.-T., Wu, Y., et al. 2015, *ApJ*, 810, 147. doi:10.1088/0004-637X/810/2/147

- McKee, C. F. & Tan, J. C. 2002, *Nature*, 416, 59. doi:10.1038/416059a
- Minier, V., Burton, M. G., Hill, T., et al. 2005, *A&A*, 429, 945. doi:10.1051/0004-6361:20041137
- Myers, A. T., McKee, C. F., Cunningham, A. J., et al. 2013, *ApJ*, 766, 97. doi:10.1088/0004-637X/766/2/97
- Moscadelli, L., Sanna, A., & Goddi, C. 2011, *A&A*, 536, A38. doi:10.1051/0004-6361/201117791
- Motte, F., Bontemps, S., & Louvet, F. 2018, *ARA&A*, 56, 41. doi:10.1146/annurev-astro-091916-055235
- Pandian, J. D., Momjian, E., Xu, Y., et al. 2011, *ApJ*, 730, 55. doi:10.1088/0004-637X/730/1/55
- Peretto, N., Fuller, G. A., Duarte-Cabral, A., et al. 2013, *A&A*, 555, A112. doi:10.1051/0004-6361/201321318
- Rodríguez-Esnard, I.T. 2011, PhD Thesis, Universidad de Guanajuato, Mexico
- Rudolph, A., Welch, W. J., Palmer, P., et al. 1990, *ApJ*, 363, 528. doi:10.1086/169363
- Sanna, A., Moscadelli, L., Cesaroni, R., et al. 2010, *A&A*, 517, A71. doi:10.1051/0004-6361/201014233
- Sanna, A., Moscadelli, L., Cesaroni, R., et al. 2010, *A&A*, 517, A78. doi:10.1051/0004-6361/201014234
- Serabyn, E., Guesten, R., & Schulz, A. 1993, *ApJ*, 413, 571. doi:10.1086/173026
- Smith, N., Whitney, B. A., Conti, P. S., et al. 2009, *MNRAS*, 399, 952. doi:10.1111/j.1365-2966.2009.15343.x
- Stahler, S. W., Shu, F. H., & Taam, R. E. 1980, *ApJ*, 241, 637. doi:10.1086/158377
- Takefuji, K., Imai, H., & Sekido, M. 2016, *PASJ*, 68, 86. doi:10.1093/pasj/psw077
- Welch, W. J., Dreher, J. W., Jackson, J. M., et al. 1987, *Science*, 238, 1550. doi:10.1126/science.238.4833.1550
- Welch, W. J., Vogel, S. N., Plambeck, R. L., et al. 1985, *Science*, 228, 1389. doi:10.1126/science.228.4706.1389
- Wilner, D. J., De Pree, C. G., Welch, W. J., et al. 2001, *ApJ*, 550, L81. doi:10.1086/319498
- Zhang, B., Reid, M. J., Menten, K. M., et al. 2013, *ApJ*, 775, 79. doi:10.1088/0004-637X/775/1/79
- Zinnecker, H. & Yorke, H. W. 2007, *ARA&A*, 45, 481. doi:10.1146/annurev.astro.44.051905.092549

A Model of ellipse

To test if the observed positions of the maser spots fit into a model of an ellipse, the equation of the conic is used, given as follows:

$$G = a_{11}x_i^2 + a_{12}x_iy_i + a_{22}y_i^2 + a_{01}x_i + a_{02}y_i + a_{00}, \quad (1)$$

where x_i and y_i are, respectively, the observed RA and observed Dec. of the spots. The coefficients a_{ij} determine the output parameters of the geometric model. The second-degree coefficients a_{11} , a_{22} , and a_{12} , determine whether the function is an ellipse or not, a_{12} is the rotation coefficient, while a_{01} and a_{02} are the translation coefficients (Apostol 2001). Furthermore, we provide a basis for testing whether the spot locations can fit an ellipse, based on Equation 1.

In the teohterical case, for a non-degenerate conic, $G=0$. In an experimental situation, the better a model fits the observed values (x_i and y_i), the smaller will be G . Then, the coefficients have to be selected such that G takes the smallest possible value. To find the a_{ij} values that lead to the best fit, the least-squares method is used. With this purpose, the python function *leastsq* is applied, from the *optimize* package inside the *scipy* python module and *pylab* interface for the use of the *matplotlib* library. To find the coefficient for the best fit, at least six spots are needed.

The least-squares method minimizes the value of S^2 , given by:

$$S^2 = \frac{1}{N - N_p} \sum_i^N \frac{G^2}{\epsilon_i^2}, \quad (2)$$

where ϵ_i is the estimated uncertainty given as $\epsilon_i^2 = \epsilon_{ix}^2 + \epsilon_{iy}^2$, with ϵ_{ix} the uncertainty in x_i and ϵ_{iy} the uncertainty in y_i , N_p is the number of parameters for the fit, N is the total amount of spots, and $N - N_p$ is the number of degrees of freedom.

The Equation 1 can be expressed in matrix form as:

$$G = \begin{pmatrix} 1 & x & y \end{pmatrix} \begin{bmatrix} a_{00} & \frac{a_{01}}{2} & \frac{a_{02}}{2} \\ \frac{a_{10}}{2} & a_{11} & \frac{a_{12}}{2} \\ \frac{a_{20}}{2} & \frac{a_{21}}{2} & a_{22} \end{bmatrix} \begin{pmatrix} 1 \\ x \\ y \end{pmatrix} \quad (3)$$

and the matrix will be further referred to as A , which can be expressed as:

$$A = \sum_{i=0}^2 \sum_{j=0}^2 a_{ij} = \begin{bmatrix} a_{00} & \frac{a_{01}}{2} & \frac{a_{02}}{2} \\ \frac{a_{10}}{2} & a_{11} & \frac{a_{12}}{2} \\ \frac{a_{20}}{2} & \frac{a_{21}}{2} & a_{22} \end{bmatrix}. \quad (4)$$

The condition for a non-degenerate conic is that $\det(A) \neq 0$ and the condition for having an ellipse is that $4a_{11}a_{22} - a_{12}^2 > 0$. From A , we can take a submatrix A_0 as follows

$$A_0 = \begin{bmatrix} a_{11} & \frac{a_{12}}{2} \\ \frac{a_{21}}{2} & a_{22} \end{bmatrix}. \quad (5)$$

Then, considering that $a_{12} = a_{21}$, the condition for an ellipse is $\det(A_0) > 0$. Further, a description of the process to find the elements of an ellipse is made. It is based on Apostol (2001), where similar cases are studied ¹. The reduced equation of the ellipse (from the general Equation 1), after a rotation and a translation, is:

$$\lambda_1 x'^2 + \lambda_2 y'^2 + g_{00} = 0, \quad (6)$$

where x' and y' are the rotated values (from observed RA and Dec., respectively), λ_1 and λ_2 are the eigenvalues of A_0 (here, λ_1 is the eigenvalue with the lowest absolute value, since it is inversely proportional to a , with a as the major semiaxis, and λ_2 is inversely proportional to the minor semiaxis, b), and g_{00} is given by:

$$g_{00} = \frac{\det(A)}{\det(A_0)}. \quad (7)$$

If Equation 6 is divided by $-g_{00}$ we obtain

$$\frac{\lambda_1 x'^2}{-g_{00}} + \frac{\lambda_2 y'^2}{-g_{00}} - 1 = 0. \quad (8)$$

Equation 8 can be expressed in a convenient form to get it in the standard ellipse formula, as follows:

$$\frac{x'^2}{\left(\sqrt{-\frac{g_{00}}{\lambda_1}}\right)^2} + \frac{y'^2}{\left(\sqrt{-\frac{g_{00}}{\lambda_2}}\right)^2} = 1. \quad (9)$$

To diagonalize A_0 and eliminate the rotation terms, with the aim to determine the eigen values, λ_1 and λ_2 , the following equation is used (Apostol 2001):

$$\det(\lambda I - A_0) = \lambda^2 - \text{Tr}(A_0)\lambda + \det(A_0), \quad (10)$$

where I is the identity matrix and $\text{Tr}(A_0)$ is the trace of the matrix A_0 . The solution of the quadratic Equation 10 yields two values, namely, λ_1 and λ_2 . On the other hand, it may be seen from Equation 9 that the minor and major axis are given in terms of the eigen values as:

$$a = \sqrt{-\frac{g_{00}}{\lambda_1}} \quad (11)$$

and

$$b = \sqrt{-\frac{g_{00}}{\lambda_2}}, \quad (12)$$

¹The involved equations are given in sections "Reduction from a real quadratic form to a diagonal form", "Applications to analytical geometry" and in a number of examples and exercises.

where the eigenvalues λ_1 and λ_2 are found from Equation 10 by using the A_0 matrix and, consequently, the a_{ij} values that lead to the minimum of S^2 in Equation 2. These are the values that give the ellipse of the best fit.

The centre of the ellipse, (x_0, y_0) , can be found from Equation 1. Substituting the translation equations $x = x' + x_0$ and $y = y' + y_0$ into Equation 1, and assuming it equals zero, we have:

$$0 = a_{11}x_i'^2 + a_{12}x_i'y_i' + a_{22}y_i'^2 + (a_{10} + 2a_{11}x_0 + a_{12}y_0)x_i' + (a_{20} + a_{21}x_0 + 2a_{22}y_0)y_i' + g_{00}. \quad (13)$$

Then, setting the terms related to the translation equal to zero, that is, the coefficients of x' and y' , it follows that

$$a_{10} + 2a_{11}x_0 + a_{12}y_0 = 0 \quad (14)$$

and

$$a_{20} + a_{21}x_0 + 2a_{22}y_0 = 0. \quad (15)$$

The values of x_0 and y_0 can be found by using the values of the model of the ellipse, which lead to the best fit, then solving the system of Equations 14 and 15, which correspond, respectively, to the second and third rows of the matrix A .

Finally, the inclination angle (θ) is given as (Wooton 1985):

$$tg(2\theta) = \frac{a_{12}}{a_{11} - a_{22}}, \quad (16)$$

which can be found by using the values for the best fit.